# Motion Blur Identification from Image Gradients

Hui Ji
Department of Mathematics
National University of Singapore
Singapore, 117542
matjh@nus.edu.sg

Chaoqiang Liu
Center for Wavelets, Approx. and Info. Proc.
National University of Singapore
Singapore, 117542
tslliucq@nus.edu.sg

## Abstract

*Restoration of a degraded image from motion blurring is highly dependent on the estimation of the blurring kernel. Most of the existing motion deblurring techniques model the blurring kernel with a shift-invariant box filter, which holds true only if the motion among images is of uniform velocity. In this paper, we present a spectral analysis of image gradients, which leads to a better configuration for identifying the blurring kernel of more general motion types (uniform velocity motion, accelerated motion and vibration). Furthermore, we introduce a hybrid Fourier-Radon transform to estimate the parameters of the blurring kernel with improved robustness to noise over available techniques. The experiments on both simulated images and real images show that our algorithm is capable of accurately identifying the blurring kernel for a wider range of motion types.*

## 1. Introduction

Motion blur is caused by the relative motion between the camera and the pictured object during the time the shuttle is open. As blurring can significantly degrade the visual quality of images, many researchers have been working either on preventing motion blurring during image capturing or on post-processing of the image to remove motion blur. For uniform motion blur, the process of blurring is usually modeled as the following convolution:

$$I(x, y) = (J * P)(x, y) + N(x, y), \tag{1}$$

where $*$ is the convolution operator, $J$ is the original image, $I$ is the degraded image and $P$ is the blurring kernel (Point Spread Function), and $N$ is the noise. To restore the original image $J$ from its blurred version $I$ using so-called image deconvolution technique, identify the blurring kernel $P$ is the first and the most important recovery step.

Early research on restoration of blurred images usually uses only a single blurred image. A prior parametric knowledge of the blurring kernel $P$ is then required to estimate the parameters of $P$. The inspection of zero patterns of the blurred image in the spectral domain has been proposed ([4, 2, 15]) to find the blur extent and the blur direction of uniform velocity motion. Also, model-based least squares and maximum likelihood (ML) blur identification methods have been proposed for the identification of general symmetric, finite extent kernels ([10, 6, 12]). By auto-regressive modeling of the blurred image and assuming the noise is zero mean Gaussian, either a least squares regression is used to estimate the kernel for noiseless blurred images ([10]), or an expectation-maximization (EM) algorithm is used to compute ML parameters for noisy blurred images with medium signal-to-noise ratios ([12]).

Recently, image deblurring systems have been developed using hardware or multiple images to obtain necessary motion information in restoring degraded images. [1] uses a hybrid imaging system to find the kernel and [13] computes a binary coded exposure sequence to keep the high spatial frequencies lost in blurred images. In [9], the motion deblurring from multiple images is done by using fast image capture in CMOS. The approach in [14] restores a clear image using two images with motion blurring along perpendicular directions. Another interesting approach is to use some assumptions on the statistical property of the image gradients' distribution to either approximate the unblurred image ([3, 8, 18]), or check the property of selected blurred edges to estimate the local blurring filters ([5]).

In this paper, we focus on restoring a single motion-blurred image taken by a hand-held digital camera. And we do not make any assumption on the statistical property of the blurred image, as it does not always hold in real life. Most available techniques of restoring a single blurred image assume an uniform velocity motion between the camera and the scene. However, there are many other motion types present when images are taken by a hand-held camera. Common motion types include: uniform velocity, accelerated motion and vibrations. Zero patterns of the blurred

978-1-4244-2243-2/08/$25.00 ©2008 IEEE

image in the spectral domain only appear in the case of uniform velocity motions. The assumption of the symmetry of the kernel in ML approaches also works only for uniform velocity motion. Moreover, even if the true kernel is indeed symmetric, those approaches are still very sensitive to the noise in the image.

Rosenfeld suggested in [16] that the blurring kernel of a motion-blurred image may be estimated from the blurred intensity distribution of a point object or a sharp edge against a homogeneous background. Finding such edges or point objects is definitely a challenging task. However this leads us to investigate the properties of blurred image gradients in the spectral domain. Our spectral analysis of blurred image gradients shows that there exists some stronger periodic pattern of blurred image gradients in the spectral domain. And this underlying pattern has the following desired properties:

1. It is easier to detect and is more robust to noise than the zero pattern of the blurred image intensity.

2. It holds true for both uniform velocity motions and accelerated motions.

3. It could also be used to detect the motion blurring by the vibration.

Another contribution in this paper is the introduction of a hybrid Fourier-Radon transform to find such periodic patterns in the spectral domain. Based on this new Fourier-Radon transform, we propose an algorithm to identify the blurring kernel of multiple motion types for noisy blurred images.

The rest of the paper is organized as follows: in Section 2, we first review the model of the blurring kernel of various motion types proposed in [17], followed by an analysis of blurred image gradients in the spectral domain. Section 3 introduces the Fourier-Radon transform and describes the algorithm for estimating the parameters of the blurring kernel. Experimental results are shown in Section 4 to demonstrate the effectiveness and robustness of our approach to restore motion-blurred images. At the end, we also discuss some aspects of our approach and possible future work.

# 2. Analysis of motion blurring on image gradients

## 2.1. Motion blur model

Given a motion-blurred image taken by a digital camera, we could assume the kernel $P(x, y)$ is one-dimensional if there are no significant changes in the motion direction during the exposure time. The horizontal kernel $P(x)$ can be adequately approximated by a trapezoid ([17]):

$$P(x) = c\big((1-\alpha) + \alpha(x + \frac{L}{2})\big)\chi_{[-\frac{L}{2},\frac{L}{2}]}(x), \quad (2)$$

where $\chi_{[-\frac{L}{2},\frac{L}{2}]}$ is the characteristic function on $[-\frac{L}{2}, \frac{L}{2}]$ and the constant $c$ is the normalization term such that

$$\int_{\mathcal{R}} P(x)dx = 1. \quad (3)$$

The discrete version of $P(x)$ could be written as:

$$p = c\big((1-\alpha)(1, 1, \cdots, 1) + \alpha(1, 2, \cdots, L)\big). \quad (4)$$

There are two important parameters in this horizontal model: the motion blur shape $\alpha$; and the extent or the length of the kernel $L$. Three representative prototype kernels from the model (2) are:

(i) *Ramp* for highly accelerated (or decelerated) motion with $\alpha = 1$:

$$\begin{array}{l} p = \frac{2}{L(L+1)}(1, 2, \cdots, L) \\ (\text{or } p = \frac{2}{L(L+1)}(L, \cdots, 1)). \end{array} \quad (5)$$

(ii) *Trapezoid* for accelerated (or decelerated) motion with $\alpha = \frac{1}{L+1}$:

$$\begin{array}{l} p = \frac{2}{L(3L+1)}(L+1, L+2, \cdots, 2L) \\ (\text{or } p = \frac{2}{3L+1}(2L, 2L-1, \cdots, L+1)). \end{array} \quad (6)$$

(iii) *Square plus* for uniform motion with $\alpha = 0$:

$$p = \frac{1}{L}(1, 1, \cdots, 1).$$

As far as the blur direction is concerned, the directional blurring $P_\theta(x, y)$ can be formulated by rotating the horizontal kernel $P(x)$ around $x$-axis by $\theta$ degree. Thus in our model, there are totally three quantitative parameters to estimate: motion blur shape $\alpha$, extent $L$, direction $\theta$; and one qualitative parameter to determine: accelerated or decelerated.

## 2.2. Cepstral method

The popular cepstral method ([4, 2, 15]) tries to identify blur extent and direction of uniform velocity motion by inspecting the zero pattern of the blurred image in the spectral domain. The basic idea is as follows. Consider a horizontal uniform velocity motion where $P_u = \frac{1}{L}\chi_{[-L/2,L/2]}$. By taking the Fourier transform on both sides of Eqn. 1, we obtain

$$\widehat{I} = \widehat{H}\widehat{P} + \widehat{N}, \quad (7)$$

where $\widehat{\cdot}$ is the Fourier transform defined by

$$\widehat{f}(\omega) = \int_{-\infty}^{\infty} f(x)e^{-2\pi i\omega x}dx. \quad (8)$$

Notice that the Fourier transform $\widehat{P}_u$ of $P_u$ is a sinc function:

$$\widehat{P}_u(\omega) = \frac{\sin \pi\omega L}{\pi\omega L} = sinc(\pi\omega L). \quad (9)$$

with periodic zeros $\{x = \frac{k}{L}, \quad k = 0, \pm 1, \pm 2, \cdots\}$. The same periodic zeros are still preserved in $\widehat{I}$ if we omit the noise $\widehat{N}$. The inspection of such a periodic zero pattern is usually done by using the so-called *cepstrum* of the blurred image to estimate the blur extent $L$. The *cepstrum* of the blurred image $I$ is defined as

$$\mathcal{C}(I) = \widehat{\log |\widehat{I}|}. \quad (10)$$

Notice that the cepstrum is additive under convolution, that is,

$$\mathcal{C}(I) = \widehat{\log |\widehat{H * P}|} = \widehat{\log |\widehat{H}|} + \widehat{\log |\widehat{P}|} = \mathcal{C}(H) + \mathcal{C}(P). \quad (11)$$

$\log |\widehat{P}|$ has large periodic negative spikes at $\pm\frac{1}{L}, \pm\frac{2}{L} \cdots$ with periodicity $1/L$, which is very likely preserved in $\log |\widehat{I}|$. Thus, we will see two peaks in the cepstrum $\mathcal{C}(I)$ and the distance between these two peaks is $\frac{2}{L}$. For arbitrarily oriented uniform velocity motion, the motion direction $\theta$ could be obtained from the orientation of line segment which passing through these two peaks in $\mathcal{C}(I)$.

### 2.3. Spectral analysis of image gradients

If there is little noise in the image and the motion is very close to uniform velocity, the cepstral method could identify the kernel $P$ reasonably well. However, it will fail for other motion types since there is no such zero pattern present in those cases. Even for uniform velocity motion, the fast decay of the sinc function could make the inspection of the zero pattern very difficult for noisy images. It turns out that there also exists a similar periodic pattern of blurred image gradients in the spectral domain. The new periodic pattern is much easier to inspect and more robust to the noise.

For the simplicity of the discussion, we first assume that the blur direction is horizontal. The differentiation on both sides of Eqn. 1 yields

$$I' = (H * P)' + N'. \quad (12)$$

Omitting the noise term $N'$, we have

$$\widehat{I'}(\omega) = \widehat{(H * P)'}(\omega) = \widehat{H * P'}(\omega) = \widehat{H}(\omega)\widehat{P'}(\omega). \quad (13)$$

Based on the definition of $P(x)$ in Eqn. 2, $|\widehat{P'}(\omega)|$ could be expressed as:

$$\begin{aligned} |\widehat{P'}| &= |i2\pi\omega\widehat{P}(\omega)| \\ &= C|\alpha(-Le^{-iL\pi\omega} + \tfrac{\sin(L\pi\omega)}{\pi\omega}) + 2(1-\alpha)i\sin(L\pi\omega)| \\ &= C\big((2+\alpha(L-2))^2\sin^2(L\pi\omega) + \alpha^2L^2\cos^2(L\pi\omega) \\ &\quad -\tfrac{\alpha^2}{\pi\omega}(L\sin(2L\pi\omega)) + \tfrac{\alpha^2}{\pi^2\omega^2}\sin^2(L\pi\omega)\big)^{\frac{1}{2}}. \end{aligned} \quad (14)$$

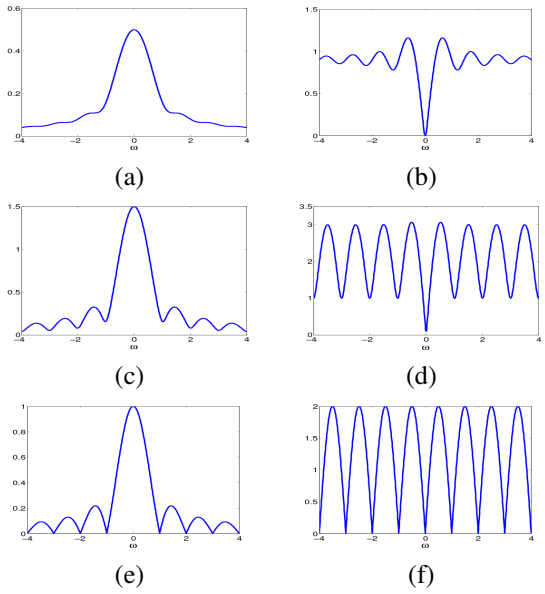

Figure 1. (a),(c),(e) are $|\widehat{P}(\omega)|$ of the kernel $P$ in the spectral domain for motion type (1) Ramp, (2) Trapezoid and (3) Square plus respectively; (b), (d), (f) are $|\widehat{P'}(\omega)|$ of the kernel $P'$ in the spectral domain for motion type (1), (2), (3) respectively.

for some constant $C$. $|\widehat{P'}(\omega)|$ could be further simplified as:

$$|\widehat{P'}(\omega)| = \big(C_1\alpha^2 - C_2(1-\alpha)\sin^2(L\pi\omega) + \alpha^2 O(\frac{1}{\omega})\big)^{\frac{1}{2}}, \quad (15)$$

where

$$C_1 = CL^2, \quad C_2 = 4C(1+\alpha(L-1)). \quad (16)$$

Eqn. 15 tells us that there exists a periodic pattern of small values in $|\widehat{P'}(\omega)|$ with reasonably large $\omega$ ($\omega > \frac{1}{L}$ is enough in practice). The periodicity of this pattern is determined by the blur extent $L$. We could then expect that there exist large periodic negative spikes with periodicity $\frac{1}{L}$ in $\log |\widehat{I'}|$. The inspection of peaks in the cepstrum $\mathcal{C}(I')$ will then tell us the blurring extent $L$.

Fig. 1 compares $|\widehat{P}|$ against $|\widehat{P'}|$ for three representative motion types: ramp; trapezoid and square plus. $|\widehat{P'}|$ clearly has a much stronger periodic pattern of local small values than $|\widehat{P}|$ for all three motion types. Especially for ramp motion (highly accelerated motion), there is hardly any periodic pattern in $|\widehat{P}|$ while $|\widehat{P'}|$ still has a noticeable periodic pattern of small values when $\omega$ is away from the original point.

The preferred periodic pattern introduced in $\log |\widehat{P'}|$ leads to a much easier identification of peaks in the cepstrum $\mathcal{C}(I')$. As a visual illustration, we compared $\log |\widehat{I'}|$ against $\log |\widehat{I}|$ of blurring images shown in Fig. 2. Fig. 3 shows that $\log |\widehat{I'}|$ clearly has a stronger periodic pattern

Figure 2. (a) is the un-blurred image; (b) is the image blurred by uniform velocity motion; (c) is the image blurred by accelerated motion; (d) is the image blurred by highly accelerated motion. All three images are blurred by a blurring kernel with the same extent (20 pixels) and the same direction (diagonal).

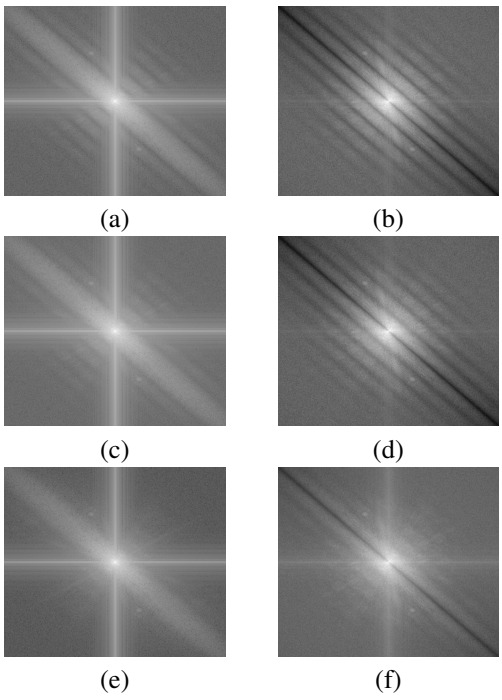

Figure 3. (a), (c), (e) are $|\widehat{I}(\omega)|$ of blurred images $I$ in Fig. 2 (b), (c), (d) respectively; (b), (d), (f) are $|\widehat{I'}(\omega)|$ of blurred image gradients $I'$ in Fig. 2 (b), (c), (d) respectively.

than $\log|\widehat{I}|$ does for these three motion types. In particular for ramp motion, we observe from Fig. 4 that the cepstrum $\mathcal{C}(I')$ can identify both the blur extent and the blur direction very well while the cepstrum $\mathcal{C}(I)$ fails to show any information on the blur extent or the blur direction.

Figure 4. (a) is the cepstrum $\mathcal{C}(I)$ of the blurred image $I$ in Fig. 2 (d) with ramp motion; (b) is the cepstrum $\mathcal{C}(I')$ of the blurred image gradients $I'$ in Fig. 2 (d) with ramp motion.

Furthermore, the phase of the peaks in the cepstrum $\mathcal{C}(I')$ tells us something about the type of the motion. It is difficult to derive a close-form for the relationship between the phase of the peaks in the cepstrum and the exact value $\alpha$. A numerical approximation shows that the phase is monotonically increasing with respect to $\alpha$. The Larger the motion shape $\alpha$ is, the farther the phase is away from $0$. The phase of the peak in $\mathcal{C}(I')$ is about $\frac{\pi}{2L}$ for ramp motion; while the phase is close to $0$ for both trapezoid motion and square plus motion. Thus we could identify the ramp motion from the phase of the peaks in the cepstrum. Combined with the analysis of the intentional restoration errors proposed in [17], we could qualitatively identify all three basic motion types: ramp; trapezoid and square plus. Whether the motion is accelerated or decelerated could also be determined from the analysis of the intentional restoration errors. In practice, it often turns out that a qualitative evaluation on $\alpha$ is good enough for restoring the blurred image.

## 3. Algorithm of identifying the blurring kernel

The cepstral method estimates the parameters of the blurring kernel $P$ by inspecting the two pronounced peaks in the cepstrum $\mathcal{C}(I')$, as shown in Fig. 4. The distance between two peaks determines the blur extent, the orientation of the straight line passing through two peaks determines the blur direction, and the phase of two peaks together with the intentional restoration residual determines the motion type. However, the main drawback of this method is that it is very sensitive to the noise in image or to the imperfect modeling of motion (moving objects in the scene, complicated motion path, etc). The peaks are often very vague in these cases. Furthermore, spurious peaks are very likely to appear in the cepstrum which make finding the correct peaks impossible. It is shown in [7] that the estimation of motion direction using the cepstral method is very poor for noisy blurred images.

The Radon transform is widely used to extract straight line features from noisy images. The Radon transform is

defined by

$$\mathcal{R}(I)(\rho,\theta)=\int_{-\infty}^{\infty} I(\rho\cos\theta-s\sin\theta,\rho\sin\theta+s\cos\theta)ds, \tag{17}$$

which integrates $I$ over a line of distance $\rho$ from the origin and at an angle $\theta$ to the $y$-axis. It is easy to see that any line in the image will be represented by a peak in the Radon transform whose location determines the parameters of the line in the original image.

Recall that given a motion-blurred image, we have periodic large negative lines in $\log|\widehat{I'}|$ with slope $\theta_0$ and periodicity $\frac{1}{L}$, as shown in Fig. 3. So the image $\mathcal{R}(\log|\widehat{I'}|)(\rho,\theta)$ resulted from a Radon transform on $\log|\widehat{I'}|$ will have periodic peaks located at

$$(\pm\frac{1}{L},\frac{\pi}{2}-\theta_0),(\pm\frac{2}{L},\frac{\pi}{2}-\theta_0),\pm\frac{3}{L},\frac{\pi}{2}-\theta_0),\cdots. \tag{18}$$

Based on this observation, we introduce a *Fourier-Radon* transform $\mathcal{F}(\cdot)$ as follows:

$$\begin{aligned}&\mathcal{F}(g)(\omega,\theta)=\widehat{\mathcal{R}(g)}(\omega,\theta)\\&=\int_{-\infty}^{\infty}\int_{-\infty}^{\infty}e^{-2\pi i\omega\rho}g(\rho\cos\theta-s\sin\theta,\rho\sin\theta+s\cos\theta)d\rho ds.\end{aligned} \tag{19}$$

It is easy to see that there is a peak in $|\mathcal{F}(g)|$ and its location $(\omega_0,\psi_0)$ is determined by the blur extent $L$ and the blur direction $\theta_0$ as follows:

$$\omega_0=\frac{1}{L}\quad\text{and}\quad\psi_0=\frac{\pi}{2}-\theta_0. \tag{20}$$

**Theorem 3.1** *Let $g(x,y)$ be the image of periodic lines of slope $\frac{\pi}{2}-\theta_0$ defined by*

$$g(x,y)=\sum_{k\in\mathbb{N}}\chi(Lk-x\cos\theta_0-y\sin\theta_0), \tag{21}$$

*where $\chi$ is the characteristic function on $0$ and $L$ is the periodicity. Then we have*

$$\mathcal{F}(g)(\omega,\theta)=\delta(\omega-\frac{1}{L})\chi(\theta-\theta_0),\quad\theta\in[0,\pi), \tag{22}$$

*where $\delta$ is the Dirac delta distribution.*

See Appendix A for the proof.

The incorporation of the Radon transform into the estimation of motion blur direction is not new. In [7], the blur direction is first estimated by identifying the peak in Radon transform. Then the blur extent is estimated from the 1D cepstrum of the de-rotated blurred image based on the estimated motion direction. The drawback of this sequential approach is that the periodicity of large negative lines in $\log|\widehat{I}|$ are not enforced in an optimal way. On the contrary, our proposed Fourier-Radon transform leads to a more robust estimation on the blur extent and the blur direction by simultaneously estimating these two parameters and by enforcing the periodicity constraint.

It is noted here that the Fourier-Radon transform may not be a good choice if it is applied directly on $\log|\widehat{I}|$ as most approaches do. The reason is that the periodicity in $\log|\widehat{I}|$ is very weak for non-uniform velocity motions. It is then not a good constraint to enforce in the estimation process. However, it is not the case if we use $\log|\widehat{I'}|$ of the image gradients. The Fourier-Radon transform could be used to explore the potential brought on by the strong periodicity of large negative lines in $\log|\widehat{I'}|$. At the end, a detailed description of the algorithm is given as follows.

Given a blurred image $I$,

1. Calculate four image gradients $I'_1,I'_2,I'_3,I'_4$ of the blurred image $I$ on horizontal direction, vertical direction, diagonal direction, anti-diagonal direction respectively.
2. For each $I'_k$, calculate $\log|\widehat{I'_k}|$.
3. For each $I'_k$, compute the Fourier-Radon transform $\mathcal{F}(\log|\widehat{I'_k}|)$ using Eqn. 19.
4. Find $M$ points $\{(\omega_k,\theta_k),k=1,\cdots,M\}$ corresponding to $M$ largest values of $\sum_{k=1}^{4}|\mathcal{F}(\log|\widehat{I'_k}|)|$.
5. From each point $(\omega_i,\theta_i)$ and its corresponding phase $Arg(\sum_{k=1}^{4}\mathcal{F}(\log|\widehat{I'_k}|)(\omega_i,\theta_i))$, derive the parameters of each kernel candidate: the extent $L_i$, the direction $\theta_i$ and the motion type.
6. For each blurring kernel candidate, deblur the image $I$ by the total variation deconvolution algorithm from [11].
7. Use the analysis technique on intentional restoration error ([17]) to find the most likely kernel and its restored image.

# 4. Experiments and conclusions

## 4.1. Simulated noisy images

In the first experiment, we use the image shown in Fig. 2 (a) as the original image to synthesize the blurred images of three motion types (ramp, trapezoid and square plus) with different noise levels. The purpose of this experiment is to evaluate the robustness to noise of our proposed approach against available approaches. For the comparison, we choose the algorithm proposed in [7] which sequentially combines the Radon transform and 1D cepstral method. The reason why we choose this algorithm is that it generally outperforms the traditional 2D cepstral method by a large margin, especially on the estimation of motion direction.

(a) (b)

Figure 5. (a) is the noisy version of the blurred image shown in Fig. 2 (b) with SNR 20. (b) is the noisy version of the blurred image shown in Fig. 2 (b) with SNR 12.

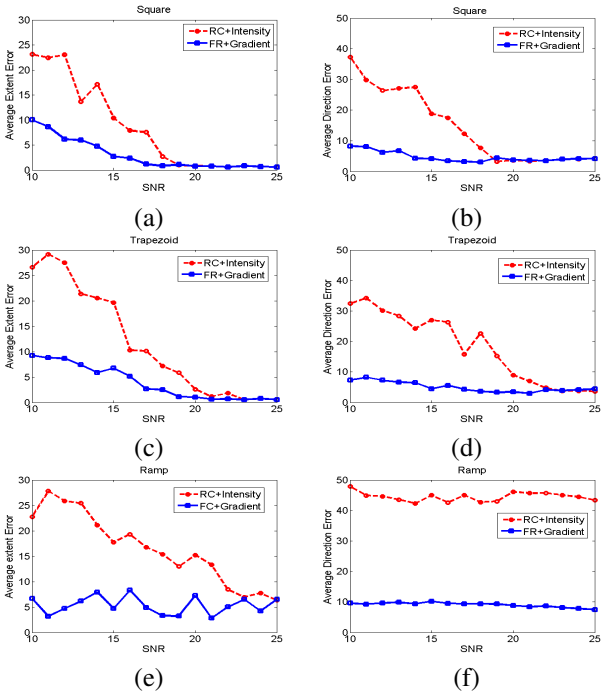


Figure 6. (a), (c) and (e) are the average estimation errors of blur extent for three motion types: ramp, trapezoid and square plus respectively; (b), (d) and (f) are the average estimation errors of blur direction for three motion types: ramp, trapezoid and square plus. 'RC+Intensity' denotes the method in [7]. 'FR+Gradient' denotes our method.

And the blur direction is more important than other parameters when we restore the blurred image using the estimated blurring kernel.

All blurred images in this experiment are generated by applying a blurring kernel with extent $L = 20$ pixels and direction $\theta = 45$ degree, subsequently contaminated by zero mean white Gaussian noise with different noise levels. Thirty two random samples are generated for each noise level. The noise level is measured by the SNR (signal-to-noise ratio) of the noised image $\tilde{I}$ to the true image $I$, which

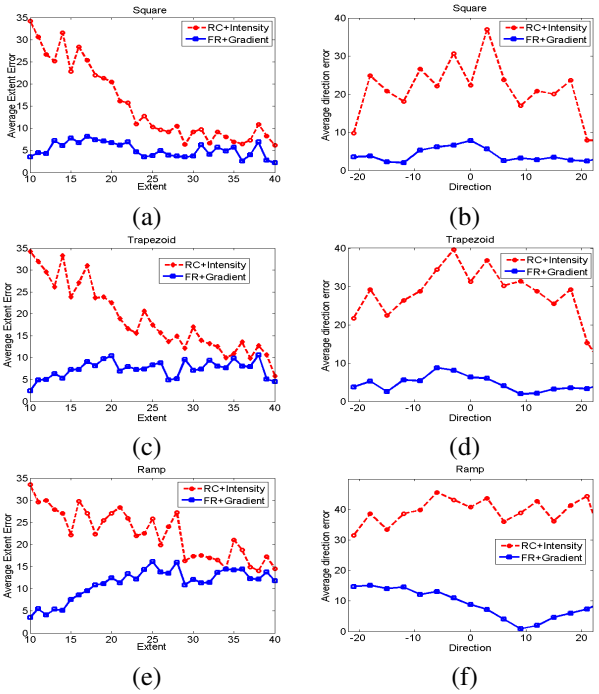


Figure 7. (a), (c) and (e) are the average estimation errors of blur extent for three motion types. The corresponding blurring directions are all 45 degree. (b), (d) and (f) are the average estimation errors of blur direction for three motion types. The corresponding blur extents are all 20 pixels. 'RC+Intensity' denotes the method in [7] and 'FR+Gradient' denotes our method.

is defined as

$$SNR(I) = 20\log_{10}(\|I\|_2/\|I - \tilde{I}\|_2). \qquad (23)$$

See Fig 5 for two noisy samples of the blurred image shown in Fig. 2 (b).

Fig. 6 compares the results from our method (denoted by FR+Gradients method) against those from the algorithm in [7] (denoted by RC+Intensity method) with different noise levels. The comparison shows that our algorithm is more robust to noise than the algorithm in [7] on the estimation of both the blur extent and the blur direction for all three motion types. In particular, [7] completely fails on the estimation of the blur direction of the ramp motion even when the noise level is low, while the noise hardly has any impact on the estimation of the blur direction by our algorithm. The robustness of our method relies mostly on the stronger periodic patterns which cancel the increasing noise level when use image gradients compared to using image intensities. Also, the introduced Fourier-Radon method can detect such periodicity better than ceptral methods do, since it simutaneously utilizes both parallelity and periodicity instead of sequentially using them as ceptral methods do.

Fig. 7 compares the performance of two methods on images blurred by different blurring kernels with strong noise.


Figure 8. (a), (d) and (h) are three real motion-blurred images; (b), (e) and (i) are the de-blurred images using the blurring kernel estimated by the method in [7] and (c), (f) and (j) are the deblurred image using the blurring kernel estimated by our method. All blurred images are restored by the deconvolution algorithm presented in [11].

The tested images are simulated by applying blur kernels of different directions and different extents on the original image shown in Fig. 2 (a). The SNRs of all tested images are 12 dB. The blur direction ranges from -22.5 degree to 22.5 degree; and the blur extent ranges from 10 pixels to 40 pixels. The results from two methods are shown in Fig. 7. It is clear that out algorithm outperforms the algorithm in [7] by a large margin both on the estimation of the blur extent and on the estimation of the blur direction.

### 4.2. Real images

In the second experiment, we run both algorithms on 100 real images of both indoor and outdoor scenes. All images are taken by a hand-held digital camera without stabilizing the camera body. First both methods are applied on the blurred images to identify the blurring kernel. Then the deconvolution algorithm in [11] is implemented to restore the blurred images. The de-blurred images of all images by both algorithms are visually evaluated. If the de-blurred image bring noticeable visual improvement over blurred image, we call it 'successful'; otherwise we call it 'unsuccessful'. Among all 100 tested images, 73 images are successfully restored by our method but only 44 images are successfully restored by the algorithm in [7]. Fig. 8 lists three samples. The left column of Fig. 8 shows three blurred images. The middle and the right column of Fig. 8 demonstrate the corresponding de-blurred images using [7] and our method respectively. The visual improvement of our algorithm over [7] is evident in all three samples.

### 4.3. Conclusion and future work

From the results of both simulated and real images, we could clearly see the advantage of our approach over available techniques. By working on the image gradients, we obtain a periodic pattern which exists in a wide range of motion types and robust to noise. Also, the proposed Fourier-Radon transform provides a robust algorithm to catch this periodic pattern even in noisy images. In our experiment, it turns out that the blurred image due to camera shakes often can not be modeled well by an uniform velocity motion blurring. Instead, a trapezoid motion or a ramp motion is a better description of camera shakes. Also, the motion blurring of the object is often accompanied by the out-of-focus blurring of the background. Our algorithm still can find the

motion-blurring kernel in many cases while the other techniques can not. In future, we would like to investigate the generalization of our algorithm to handle more complicated motion blur. In particular, we are interested in developing a localize version of our algorithm to identify the block-wise blurring kernels of a given blurred image. With such an algorithm in hand, we will be able to restore the motion-blurred image caused by fast-moving objects in the scene.

## Acknowledgments

This work was partially supported by NUS ARF under grant number R-146-050-091-101 and R-146-050-091-133. The second author would like to thank DSTA funding for support of the programme "Wavelets and Information Processing".

## References

[1] M. Ben-Ezra and S. K. Nayar. Motion-based motion deblurring. *IEEE Trans. PAMI*, 26(6):689–698, 2004.

[2] M. Cannon. Blind deconvolution of spatially invariant image blurs with phase. *IEEE Trans. Acoust. Speech, Signal Processing*, 24:58–63, 1976.

[3] R. Fergus, B. Singh, A. Hertzmann, S. T. Roweis, and W. T. Freeman. Removing camera shake from a single photograph. In *SIGGRAPH*, volume 25, pages 783–794, 2006.

[4] D. B. Gennety. Determination of optical transfer function by inspection of frequency-domain plot. *J. Opt. Soc,Amer.*, 63:1571–1577, Dec. 1973.

[5] J. Jia. Single image motion deblurring using transparency. In *CVPR*, 2007.

[6] A. K. Katsaggelos and K. T. Lay. Likelihood identification and restoration of images using expectation-maximization algorithm. In A. Katsaggelos, editor, *Digital Image Restoration*, pages 143–176. Springer-Verlag, 1991.

[7] F. Krahmer, Y. Lin, B. Mcadoo, K. Ott, J. Wang, D. Widemann, and B. Wohlberg. Blind image deconvolution: Motion blur estimation. In *IMA Preprints Series*, 2133-5. IMA, Sep 2006.

[8] A. Levin. Blind motion deblurring using image statistics. In *NIPS*, Dec. 2006.

[9] X. Liu and A. Gamal. Simultaneous image formation and motion blur restoration via multiple capture. In *Int. Conf. Acoustics, Speech, Signal Processing*, 2001.

[10] A. M.Tekalp, H. Kaufman, and J. Woods. Identification of image and blur parameters for the restoration of noncausal blurs. In *IEEE Trans, Acoust, Speech and Signal Processing*, volume 34, pages 963–972, 1986.

[11] M. K. Ng, R. H. Chan, and W. Tang. A fast algorithm for deblurring models with neumann boundary condition. *SIAM J. Sci. COMPUT.*, 21(3):851–866, 2000.

[12] G. Pavlovic and A. M. Tekalp. Maximum likelihood parametric blur identification based on a continuous spatial domain model. *IEEE Trans. Image Processing*, 1(4), Oct. 1992.

[13] R. Raskar, A. Agrawal, and J. Tumblin. Coded exposure photography: Motion deblurring via fluttered shutter. In *SIGGRAPH 25(3):795 804, 2006*, volume 25, pages 795–804, 2006.

[14] A. Rav-Acha and S. Peleg. Two motion blurred images are better than one. *Pattern Recognition Letters*, 26:311–317, 2005.

[15] I. M. Rekleitis. Steerable filters and cepstral analysis for optical flow calculation from a single blurred image. *Vision Interface*, 1:159–166, 1996.

[16] A. Rosenfeld and A. C. Kak. *Digital Picture Processing*. Academic Press, San Diego, second edition, 1982.

[17] K. Tan, H. Lim, and B. Tan. Restoration real-world motion-blurred images. In *CVGIP: Graphical Models and Image Processing*, volume 53, pages 291–299, 1991.

[18] Y. Yitzhaky, I. Mor, A. Lantzman, and N. S. Kopeika. Direct method for restoration of motion-blurred images. *J. Opt. Soc. Am.*, 15(6):1512–1519, 1998.

[19] Y. Yitzhaky, I. Mor, A. Lantzman, and N. S. Kopeika. Vibrated image restoration from a single frame. *Optical Engineering*, 38(8), 2000.

## A. The proof of Theorem 3.1

We have that

$$\begin{aligned}\mathcal{F}(g)(\omega,\theta) &= \widehat{\mathcal{R}(g)}(\omega,\theta)\\ &= \int_{-\infty}^{\infty} e^{-2\pi i\omega\rho}d\rho \int_{-\infty}^{\infty}\sum_k \chi(Lk-(\rho\cos\theta-\\ &\quad s\sin\theta)\cos\theta_0-(\rho\sin\theta+s\cos\theta)\sin\theta_0)ds\\ &= \int_{-\infty}^{\infty} e^{-2\pi i\omega\rho}d\rho \int_{-\infty}^{\infty}\sum_k \chi(Lk\\ &\quad -\rho\cos(\theta-\theta_0)+s\sin(\theta-\theta_0))ds. \qquad (24)\end{aligned}$$

If $\theta=\theta_0$, we have then

$$\begin{aligned}\mathcal{F}(g)(\omega,\theta) &= \sum_k \int_{-\infty}^{\infty} e^{-2\pi i\omega\rho}d\rho \int_{-\infty}^{\infty}\chi(Lk-\rho)ds\\ &= \sum_k \int_{-\infty}^{\infty} e^{-2\pi i\omega\rho}\delta(\rho-Lk)d\rho\\ &= \sum_k e^{-2\pi i\omega Lk}\\ &= \delta(\omega-\frac{1}{L}). \qquad (25)\end{aligned}$$

If $\theta\neq\theta_0$, then we have

$$\begin{aligned}\mathcal{F}(g)(\omega,\theta) &= \int_{-\infty}^{\infty} e^{-2\pi i\omega\rho}d\rho\cdot 0\\ &= 0. \qquad (26)\end{aligned}$$

Thus we have

$$\mathcal{F}(g)(\omega,\theta)=\delta(\omega-\frac{1}{L})\chi(\theta-\theta_0). \qquad (27)$$

The proof is done. □